Environmental Science & Technology

pubs.acs.org/est

Article

Steric Interaction-Engineered Free Volume Network in Polyamide Nanofiltration Membranes for Ultrafast Water Purification

Kunpeng Wang, Haiyang He, Xingzhong Cao, Xiao-mao Wang,* Danyang Li, Yanling Liu, Wenkai Liu, Peng Liang, and Xia Huang*

Cite This: *Environ. Sci. Technol.* 2026, 60, 8823−8834

Read Online

ACCESS | Metrics & More | Article Recommendations | Supporting Information

ABSTRACT: Polyamide thin-film composite membranes are critically important in combating global water scarcity. However, simultaneously achieving ultrafast water permeation and high solute rejection remains challenging due to their thick, dense separation layers. Herein, we demonstrate a simple yet versatile strategy to modulate the nanostructure of the polyamide separation layer, particularly the abundance and interconnectivity of free volume, by adopting well-designed aqueous monomers. The key is introducing methyl groups onto the conventional piperazine monomers, which accelerates trans-interfacial diffusion and decreases the ensuing amidation reaction rate. This leads to the formation of a thinner separation layer composed of more linear polyamide fragments, where the methyl groups, serving as "molecular pillar" sites, weaken the intra- and interchain interactions to prevent their dense stacking, thereby creating a more interconnected free volume network. One prepared membrane exhibits a very high water permeance of 57.8 ± 2.8 L m^{-2} h^{-1} bar^{-1} along with a satisfactory per- and polyfluoroalkyl substance rejection over 90%, as well as superior resistance to compression. This molecular-level microstructural engineering provides a new route and fundamental insights into the scalable production of high-performance separation membranes for emerging contaminant removal.

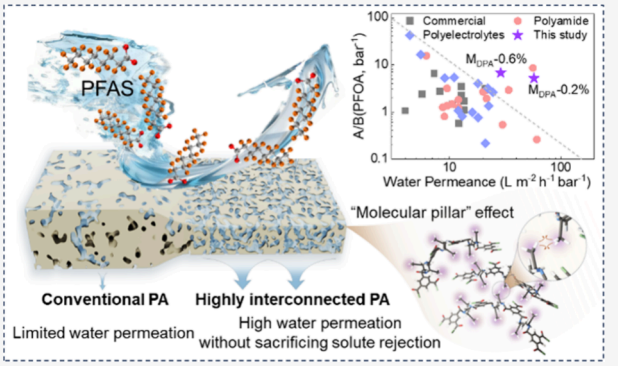

KEYWORDS: *nanofiltration, interfacial polymerization, polyamide membrane, free volume network, permeability−selectivity trade-off, PFAS removal*

INTRODUCTION

Nanofiltration (NF) membranes, characterized by their subnanometer separation precision, are pivotal for water treatment and resource recovery.[1−3] Their efficacy in removing emerging contaminants (ECs), such as per- and polyfluoroalkyl substances (PFAS), has driven extensive research and application.[4−6] These membranes are typically fabricated by forming a thin selective layer on a porous substrate via the interfacial polymerization (IP) technique. This gold-standard technique exploits the self-limiting kinetics and the self-healing nature of the in situ polycondensation reactions usually between bifunctional amines (e.g., piperazine, PIP) and trifunctional acyl chlorides (e.g., trimesoyl chloride, TMC), which results in a mechanically robust polyamide film as the selective layer with tunable separation properties.[7−9] Despite decades of significant progress, a fundamental challenge persists: the well-known trade-off effect between water permeance and solute rejection,[10,11] which severely limits the efficiency and sustainability of NF membrane processes for the removal of emerging contaminants.

Conventional strategies to break this trade-off effect have primarily focused on extrinsic morphological engineering on several nanoscales. These include reducing the selective layer thickness by constructing intermediate layers[12−15] or increasing the effective filtration area through forming crumpled surface morphologies[16−20] or incorporating nanoporous materials.[21,22] Although effective, these strategies do not substantially improve the intrinsic mass transfer properties of the polyamide material itself, limiting further performance enhancement. Recent nanoscale 3D reconstruction has revealed the internal inhomogeneity of polyamide layers, showing that water molecules preferentially permeate through low-density, high-free-volume regions.[23] This insight suggests that enhancing free volume abundance and interconnectivity can create more permeation channels, leading to intrinsically superior mass transfer properties of polyamide materials.[24−26] However, the rapid kinetics of interfacial polymerization typically trap polymer chains in a dense, nonequilibrium state, while strong interchain interactions (e.g., hydrogen

Received: November 22, 2025
Revised: March 4, 2026
Accepted: March 4, 2026
Published: March 13, 2026

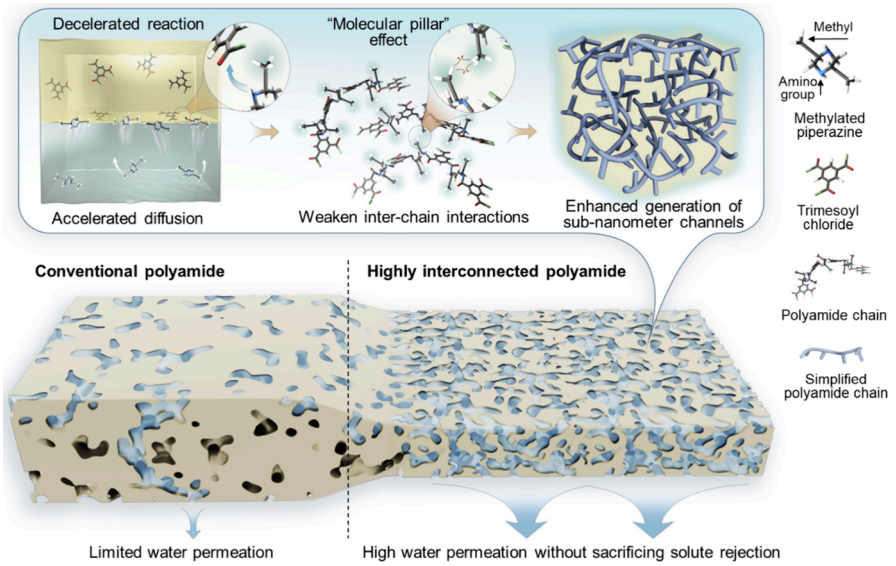

Figure 1. Schematic diagram illustrating the molecular design principle for preparing highly interconnected polyamide networks via methyl-functionalized piperazine monomers.

bonding and van der Waals forces) further promote dense packing of formed polyamide chains.[27−30] The combined effect results in a polyamide matrix with restricted free volume and poor interconnectivity, forcing water molecules to overcome successive energy barriers during permeation.[31−34] Achieving precise control of the free volume network in polyamide layer remains a significant challenge. From the perspective of the free volume formation process, attenuating dense polymer chain packing by weakening interchain interaction—for instance, through the strategic introduction of steric hindrance to hold up neighboring polymer chains—represents a promising pathway to enhance free volume abundance and interconnectivity.[35]

Herein, we propose a facile yet powerful molecular-level design strategy to precisely modulate the polyamide nanostructure, thus enhancing its intrinsic mass transfer properties and improving the removal performance of emerging contaminants. Our approach involves installing "molecular pillars" (e.g., alkyl groups) into the traditional polypiperazine-amide chains via rational design of aqueous-phase monomers for the conventional IP process (Figure 1). We hypothesize that these introduced "molecular pillar" groups will not only weaken interchain interactions in the formed polymer network via steric hindrance but also modulate IP reaction kinetics to promote chain extension and ordering, thereby ultimately yielding a more open and interconnected free volume network.[36,37] To validate this, we systematically engineered a series of methyl-functionalized piperazine monomers and investigated the effects of the number and position of the methyl groups on membrane performance. The optimized nanostructure of the polyamide selective layer significantly enhances the membrane water permeance without sacrificing the separation performance. One resulting membrane achieves a remarkable water permeance of 57.8 ± 2.8 L m^{-2} h^{-1} bar^{-1} while maintaining a satisfactory PFAS rejection over 90%. The underlying mechanisms of this nanostructure tuning, including altered monomer diffusion, reaction kinetics, and interchain interactions, are elucidated through a combination of molecular dynamics (MD) simulations and density functional theory (DFT) calculations. This study offers a novel and versatile paradigm for the precise engineering of free volume abundance and interconnectivity in synthetic membranes, effectively overcoming the longstanding permeability−selectivity trade-off for conventional membranes.

MATERIALS AND METHODS

Preparation of NF Membranes

The polyamide (PA) NF membranes were prepared directly on a polysulfone (PSf) UF membrane (MWCO 80 kDa) as a support via the IP technique (Figure 2A,B). The PSf support was first fixed on a homemade plexiglass frame (15 × 15 cm^2) and then immersed into an aqueous solution of diamine monomers for 120 s. After excess water droplets were removed from the membrane surface using a rubber roller, the UF membrane, enriched with diamine monomers, was exposed to a TMC *n*-hexane solution for 60 s to form a PA selective layer on the UF membrane. The excess TMC solution was then removed, and the nascent membrane was heat-cured in an oven at 60 °C for 5 min. Prior to testing, each prepared NF membrane was stored in deionized water at 4 °C. The TMC concentration was fixed at 0.1 wt %. Dodecyl trimethyl ammonia bromide (DTAB) with a concentration of 16 mM was added to the aqueous phase to enhance the homogeneity of the polyamide layer. The aqueous diamine monomers were PIP, 2-methylpiperazine (MPIP), and *trans*-2,5-dimethylpiperazine (DPIP), where MPIP includes both isomers R-MPIP and S-MPIP, which are not differentiated unless specified. The trans isomer of 2,5-dimethylpiperazine was used to ensure symmetric spatial effects. The PIP concentrations were 0.1, 0.2, 0.6, or 1.0 wt %, and the corresponding prepared membranes were designated as M_{PA}-0.1%, M_{PA}-0.2%, M_{PA}-0.6%, and M_{PA}-1.0%, respectively. MPIP and DPIP were used at the same molar concentrations as PIP, with membranes named M_{MPA}-0.1%, M_{MPA}-0.2%, M_{MPA}-0.6%, and M_{MPA}-1.0% and M_{DPA}-0.1%, M_{DPA}-0.2%, M_{DPA}-0.6%, and M_{DPA}-1.0%, respectively. More information on the chemicals and materials used for membrane preparation and the detailed membrane characterization are provided in Supplementary Text S1 and Text S2.

Separation Performance

The separation performance of each fabricated membrane was evaluated using a homemade cross-flow membrane filtration device with three parallel filtration cells (20.6 cm^2, CF016, Sterlitech, USA; Figure S1). All membranes were precompacted with DI water under 8 bar for 1 h to obtain stable pure water permeance. The cross-flow velocity was set at 0.20 m s^{-1}, the feedwater temperature was 25 ± 1

https://doi.org/10.1021/acs.est.5c16846
Environ. Sci. Technol. 2026, 60, 8823−8834

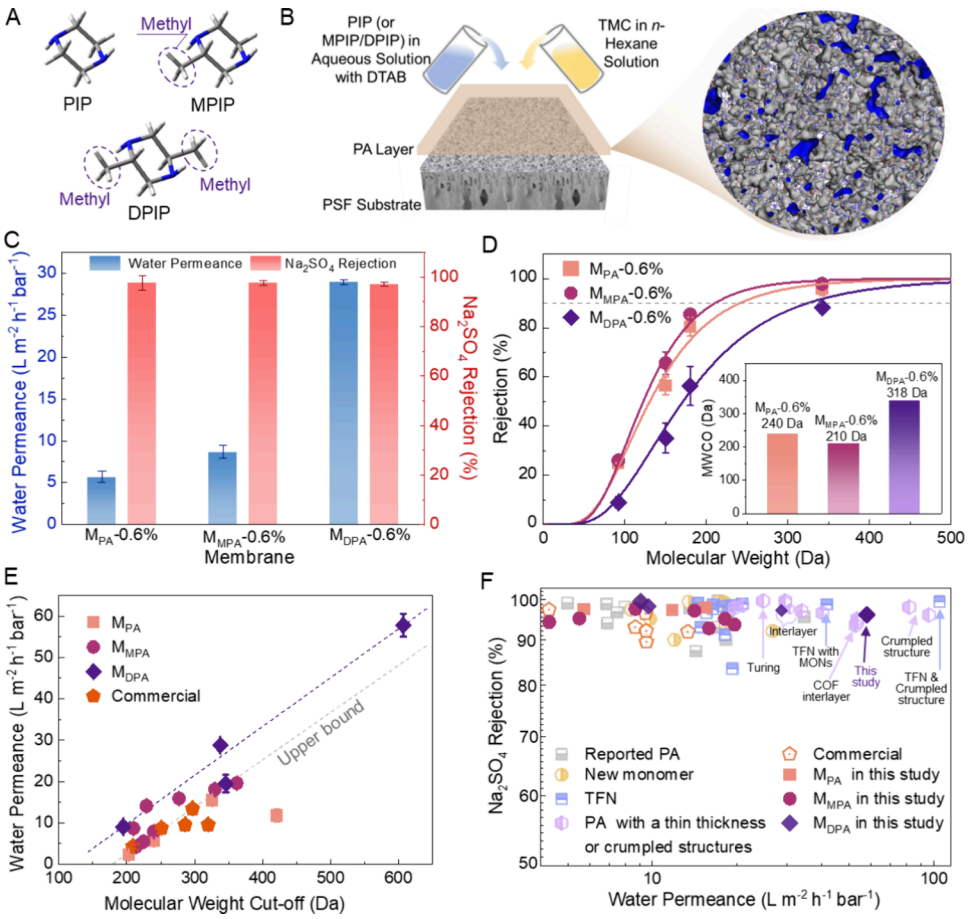

Figure 2. Synthesis of polyamide membranes via interfacial polymerization (IP) and their separation performance. (A) Reaction monomers and molecular structure, including piperazine (PIP), 2-methylpiperazine (MPIP), and *trans*-2,5-dimethylpiperazine (DPIP). (B) Schematic of the IP process between PIP (or MPIP/DPIP) and trimesoyl chloride (TMC). (C) Separation performance of the M_{PA}, M_{MPA}, and M_{DPA} membranes fabricated with an aqueous monomer concentration of 70 mM. The ionic strength of the test Na_2SO_4 solution was 10 mM. The test was conducted with an effective membrane area of 20.6 cm^2, a cross-flow velocity of 0.20 m s^{-1}, a constant applied pressure of 6 bar, a water temperature of 25.0 ± 0.5 °C, and a pH of 7.0 ± 0.1. (D) The rejections of neutral organic solutes include glycerol, D-(+)-xylose, D-(+)-glucose, and sucrose. The inset shows the molecular weight cutoff (MWCO) of the fabricated membranes by fitting rejection data. (E) Relationship between water permeance and MWCO of the membrane. The gray dashed line represents the upper bound established based on the M_{PA} membranes, with commercial membranes not going beyond this line. The purple dashed line represents the new upper bound established based on the M_{DPA} membranes. (F) Comparison of the separation performance of the fabricated membranes with those of other advanced membranes as reported in the literature.

°C, and the applied pressure was 6 bar, except for M_{DPA}-0.2% (2 bar). Each test was conducted in full circulation mode; i.e., both the permeate and concentrate were returned back to the feed tank (10 L) to maintain a constant feed concentration. Single salt solutions, each with an ionic strength of 10 mmol L^{-1} and a pH at 7.0 ± 0.1, were used to evaluate the rejection performance of membranes. For a duration of 50 h, the operational stability of M_{DPA}-0.6% at 6 bar and M_{DPA}-0.2% at 2 bar was tested. All tests on the M_{DPA}-0.2% membrane were conducted at 2 bar primarily to prevent excessive water flux from causing severe concentration polarization that would dramatically compromise the observed solute rejection. The salt concentration was measured using a conductivity meter (FiveEasy Plus FE38, Mettler Toledo). Solutions of D-(+)-xylose, D-(+)-glucose, sucrose, and raffinose were filtered to measure the MWCO and pore size of each membrane (Supplementary Text S3 and Text S4). The concentration of each small-molecule neutral organic matter was 100 mg L^{-1}, and the concentration was analyzed by using a TOC analyzer (Shimadzu TOC-VCPH, Japan). Five types of PFASs (300−500 Da), namely, perfluorobutanesulfonic acid (PFBS), perfluorohexanoic acid (PFHxA), perfluorohexanesulfonic acid (PFHxS), perfluorooctanoic acid (PFOA), and perfluorooctanesulfonic acid (PFOS), were added to the tap water for rejection tests, each at a concentration of 100 μg L^{-1}. Their molecular weights and structures are provided in the Supporting Information, Table S1. The concentration was measured using an ultraperformance liquid chromatograph−tandem mass spectrometer (LC1290/QQQ6460, Agilent). In the PFAS rejection experiment, the filtration device was stabilized for at least 8 h before sampling to ensure the PFAS adsorption reaching equilibria on the membrane.

The water permeance of the fabricated membrane was calculated using eq 1:

$$A = \frac{\Delta V}{S \Delta t \Delta P} \tag{1}$$

Here, A is the water permeance of fabricated membrane (L m^{-2} h^{-1} bar^{-1}), S is the effective filtration area, ΔP is the effective pressure on the membrane, Δt is the time duration for sample collection, and ΔV is the sampling volume.

All solute rejection rates (R) were calculated by comparing their concentrations in the feed (c_f) and the permeate (c_p) by eq 2:

$$R = \left(1 - \frac{c_p}{c_f}\right) \times 100\% \tag{2}$$

The porosity (ε) of the prepared PA layer was estimated by using the Hagen−Poiseuille equation (eq 3).

https://doi.org/10.1021/acs.est.5c16846
Environ. Sci. Technol. 2026, 60, 8823−8834

$$A = \frac{\varepsilon \alpha r_p^2}{8\mu\delta} \quad (3)$$

Here, α is the ratio of the actual area to projective area of the membrane measured by atomic force microscopy (AFM), r_p represents the average pore size calculated through the pore hindrance models, μ is the solution viscosity, and δ is the PA layer thickness obtained by AFM.

We defined the membrane separation performance index (SPI) to evaluate the intrinsic membrane permeation−rejection performance in this study, which is calculated by eq 4:

$$\mathrm{SPI} = \frac{A}{r_p^2} \quad (4)$$

The water/solute selectivity (A/B), including water/Na_2SO_4 selectivity and water/PFOA selectivity, was calculated using a simplified formula, derived from the dissolution−diffusion model, as follows:

$$R = \frac{\frac{A}{B}(P - \Delta\pi)}{\frac{A}{B}(P - \Delta\pi) + f_{cp}} \quad (5)$$

Here, R is the solute rejection rate, P is the applied pressure, $\Delta\pi$ is the bulk osmotic pressure difference across the membrane, and f_{cp} describes the effect of concentration polarization.[11,38,39]

Computational Simulation

The trans-interfacial diffusion models of different monomers were constructed using the PACKMOL program in the GROMACS 2019.6 system.[40] As shown in Figure S2, the simulation boxes (50 × 50 × 180 Å^3) were filled with water molecules (6689) in the center and *n*-hexane molecules (694) on both sides. A total of 100 diamine monomers (PIP, MPIP, or DPIP) were randomly placed in the aqueous phase, and 60 DTAB molecules were placed at the water/hexane interface according to the density of the system. The water molecule model is described using the SETTLE algorithm, while other molecules were subjected to the OPLS-AA force field and RESP charge. Energy minimization was performed using the steepest method for 10000 steps, with a convergence energy criterion set to 100 kJ/mol/nm to ensure the system reaching its most stable state. All systems were then simulated under a 200 ns NPT ensemble, using periodic boundary conditions, and the molecules' bond lengths were constrained using the LINCS algorithm.[41,42] For the NPT finished product simulation, the step size was set to 1 fs. The role of van der Waals interactions was described using the PME method (particle mesh Ewald method), with a spatial cutoff set to 1.4 nm.[43] The temperature was controlled at 300 K using the V-rescale algorithm, and the pressure was controlled at 1 bar using the Berendsen algorithm.

All molecular structures were described by using the OPLS-AA force field. Three models were generated in a cubic cell with dimensions of 10 nm for PIP-TMC, MPIP-TMC, and DPIP-TMC, with monomer ratios (total of 200) of 109:91, 108:92, and 107:93, respectively. The −H of the amino group and the −Cl of the TMC monomer were removed before the monomers were randomly placed in the cell. A new covalent bond was generated when the distance between the N− site and the O═C− site was less than 4 Å. The polymerization was iterated in several cycles until no new bonds meeting the bonding criteria were formed. The final polymer structures underwent a 21-step molecular dynamics equilibration.[44] We terminated the unreacted N− site and the O═C− site with −H and −OH after polymerization. The void structure properties, including the porosity and cavity size, were analyzed using Zeo++ software.

The reaction free energy barrier between the −NH group and the acyl chloride of TMC, as well as the polymer chains interactions, was calculated using DFT methods in the Gaussian 16 package.[45] The Becke−Lee−Yang−Parr (B3LYP) hybrid functional and the 6-311G(d,p) basis sets with D3bj were performed to optimize the reactants, reaction complex, transition state, product complex, and reaction products. Solvation effects were considered using a polarizable continuum solvent model. The stationary points were identified as either stable minima with no imaginary frequency or the transition state with only one imaginary frequency and utilized to output Gibbs free energy. The reaction free energy was obtained by differential subtraction of the free energy of the reactant state and transition state. The simulated polymer chain structures, which contained three diamine molecules and three TMC molecules, were used to evaluate the interactions within the polymer chain or between two molecular chains. The structure optimization of molecular chains was performed using the B3LYP/6-311G(d,p) method with D3bj in Gaussian 16. The optimized structure was used to analyze the weak interactions within/between molecular chains by reduced density gradient (RDG) of Multiwfn 3.8 software.[46]

RESULTS AND DISCUSSION

Membrane Separation Performance

We adopted the classical IP technique to prepare a polypiperazine-amide selective layer on a polysulfone support using different aqueous monomers. Methyl groups were introduced into the PIP monomers to form MPIP and DPIP, which are used to validate the proposed strategy of modulating the microstructure and separation performance of the conventional polypiperazine-amide membrane. The insertion of methyl groups significantly enhanced water permeance of the membrane, increasing from 5.7 ± 0.7 L m^{-2} h^{-1} bar^{-1} for M_{PA}-0.6% to 8.8 ± 0.7 L m^{-2} h^{-1} bar^{-1} for M_{MPA}-0.6% and further to 28.9 ± 0.3 L m^{-2} h^{-1} bar^{-1} for M_{DPA}-0.6% (Figure 2C). Meanwhile, the Na_2SO_4 rejection remained above 97%, confirming the formation of a defect-free polyamide separation layer, which was also verified by Fourier transform infrared spectroscopy (FTIR, Figure S3). Neutral small-molecule rejection results showed that the pore size of M_{DPA}-0.6% increased slightly with a molecular weight cutoff (MWCO) change below 100 Da (Figure 2D). These data demonstrate that methylated piperazines can significantly enhance the separation performance of conventional polypiperazine-amide NF membranes.

We further prepared a series of NF membranes by varying the concentration of aqueous-phase monomers to explore the maximum separation potential of methylated polypiperazine-amide membranes (Figures S4−S6). The optimized M_{MPA} membranes and M_{DPA} membranes can overcome the permeability−selectivity trade-off for conventional polypiperazine-amide membranes prepared under identical conditions, with the membrane selectivity represented by MWCO or pore size (Figure 2E and Figure S7). These membranes establish an elevated upper bound with tunable and excellent separation performance over a wide MWCO range (200−600 Da). The pure water permeance of M_{DPA}-0.2% was unexpectedly high, reaching 57.8 ± 2.8 L m^{-2} h^{-1} bar^{-1}, with an MWCO less than 600 Da and Na_2SO_4 rejection above 96%, which significantly outperformed the current commercial membranes always with a water permeance of 5−15 L m^{-2} h^{-1} bar^{-1} (Table S2). The optimized M_{DPA} membrane, although not the highest performance reported, demonstrated comparable or even superior water/Na_2SO_4 separation performance over the reported best-performing thin-film nanocomposite (TFN) membranes and NF membranes with interlayer or crumpled structures (Figure 2F, Table S3, and Figure S8), thus providing an additional new direction for fabricating high-water-permeance NF membranes.

https://doi.org/10.1021/acs.est.5c16846
Environ. Sci. Technol. 2026, 60, 8823−8834

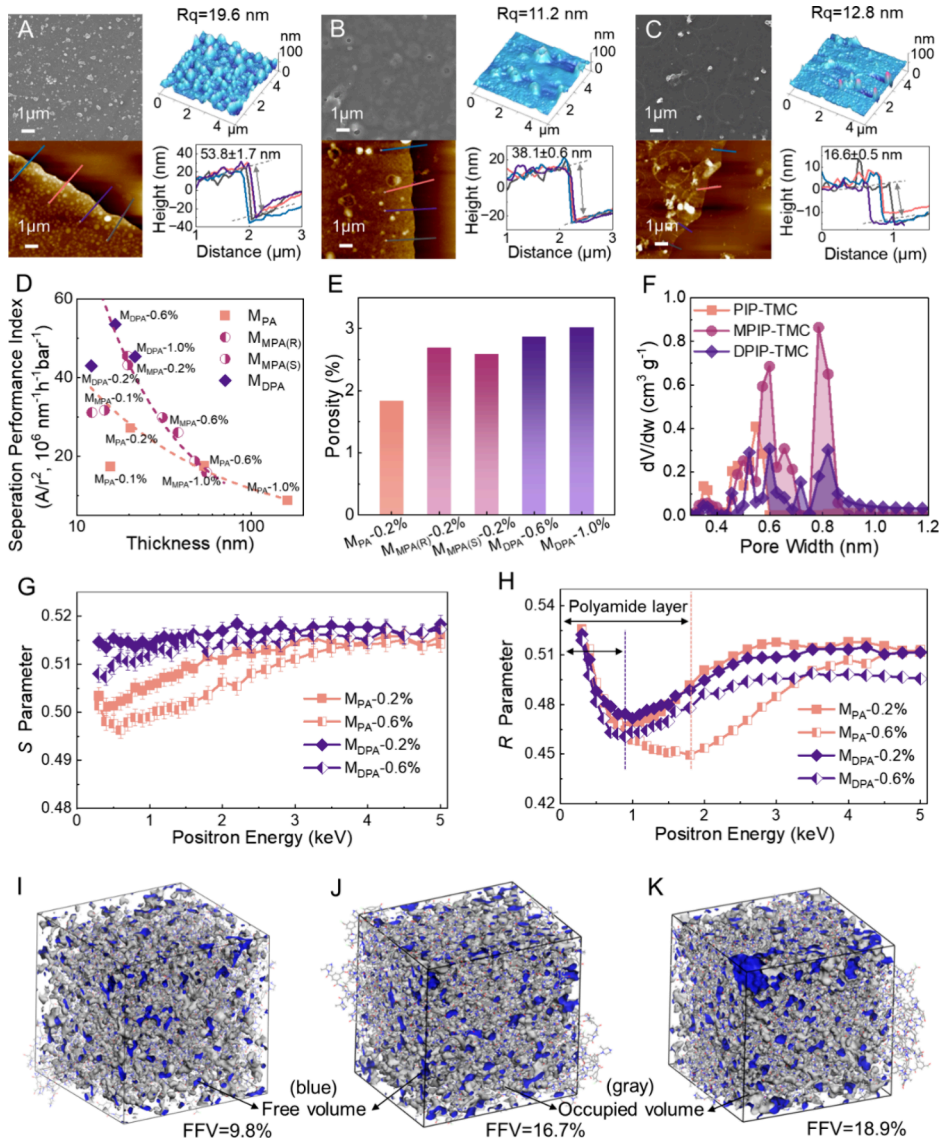

Figure 3. Structural properties of the fabricated membranes. Surface images by SEM and AFM and the selective layer thickness measured by AFM for (A) M_{PA}-0.6%, (B) M_{MPA}-0.6%, and (C) M_{DPA}-0.6%. (D) Relationship between the membrane separation performance index (SPI) and the selective layer thickness. (E) The calculated porosity of fabricated membranes with similar thickness was calculated using the Hagen−Poiseuille equation. (F) Pore size distribution of polyamide networks measured from CO_2 sorption isotherms at 273 K employing the nonlocal density functional theory (NLDFT). PAS measurements for the *S* parameter (G) and *R* parameter (H) as a function of the incident positron energy for M_{PA}-0.2%, M_{PA}-0.6%, M_{DPA}-0.2%, and M_{DPA}-0.6%. (G−I) Molecular dynamics simulation of the free volume of PIP-TMC, MPIP-TMC, and DPIP-TMC polymers. The blue and gray colors represent the voids of the polymer and the occupied space of polymer chains with a probe of 1.4 Å radius, the radius of a water molecule, respectively.

Characterization of Membrane Microstructures

To understand the enhanced separation performance resulting from the introduction of methyl groups, a systematic characterization of the physicochemical properties of the prepared membranes was conducted to reveal the properties−performance relationships. Field-emission scanning electron microscopy (FE-SEM) images and AFM images showed that the M_{PA}-0.6% membrane exhibited typical nodular structures on the surface,[16] with an average surface roughness of 19.6 ± 0.23 nm (Rq) (Figure 3A). In contrast, the M_{MPA}-0.6% and M_{DPA}-0.6% membranes exhibited smoother surfaces with less convex structures (Figure 3B,C). Although some nanorings appeared on the M_{DPA}-0.6% membrane surface, the relatively small size contributed little to the surface roughness (Figure 3C and Figure S9). The reduction in surface roughness is detrimental to water permanence due to the reduced effective permeation area.[47] However, a significant reduction in separation layer thickness, from 53.8 ± 1.7 nm for M_{PA}-0.6% to 16.6 ± 0.5 nm for M_{DPA}-0.6% (Figure 3A−C and Figure S10), effectively decreased the mass transfer resistance of water,[14] which alone could not fully explain the increased water permeance. Here, we introduced the membrane separation performance index (SPI) to evaluate the intrinsic permeability of the polyamide material. SPI is defined as the ratio of water permeance to the square of the pore radius, which normalizes the effects of pore size. We then established the relationship between SPI and the polyamide layer thickness (Figure 3D). Even at similar thicknesses (19−21 nm), the SPI of M_{MPA} and M_{DPA} membranes each was significantly higher than that of the M_{PA} membrane, indicating that the intrinsic

https://doi.org/10.1021/acs.est.5c16846
Environ. Sci. Technol. 2026, 60, 8823−8834

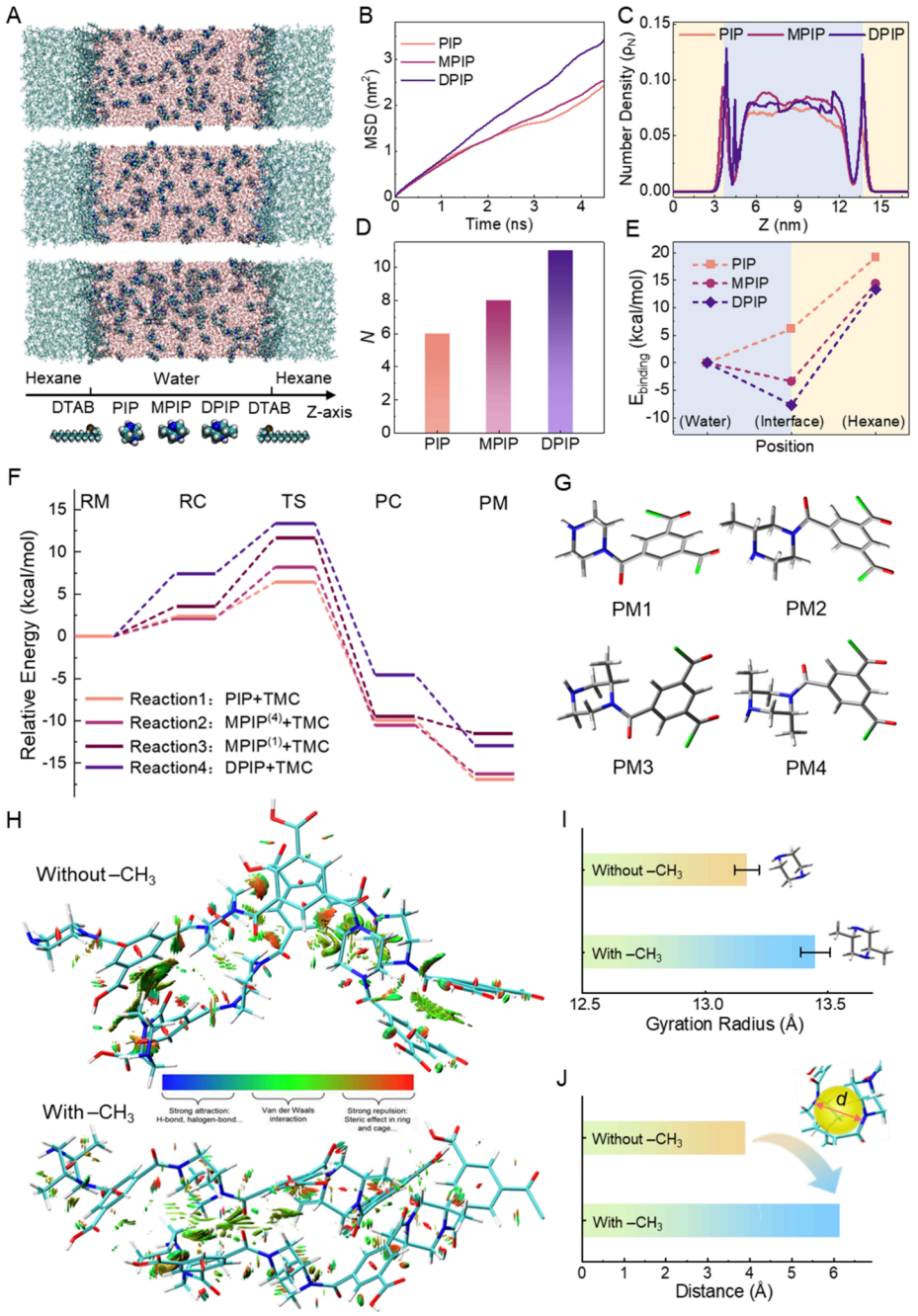

Figure 4. Modeling and simulative calculation of the interfacial polymerization process and polymer chain interactions. (A) Molecular dynamics (MD) simulation of trans-interfacial diffusion of aqueous-phase monomers (PIP, MPIP, or DPIP) in a 5 × 5 × 18 nm^3 box with the aqueous phase in the center and the hexane phase on both sides. The snapshot image is the state after diffusion stabilization. (B) Mean square displacement (MSD) profiles of PIP, MPIP, and DPIP molecules during the simulation process. (C) Number density (ρ_N) distribution of PIP, MPIP, and DPIP molecules in the Z direction. (D) Number of PIP, MPIP, and DPIP molecules at the interface after diffusion stabilization. (E) MD simulation of the binding free energy ($E_{binding}$) with the PIP, MPIP, and DPIP molecules at different positions. (F) Free energy variation for the reactions between TMC and the amine groups in the PIP, MPIP, or DPIP molecule based on DFT calculation. Each reaction is divided into five stages, namely, reaction monomers (RM), reaction complex (RC), transition state (TS), product complex (PC), and reaction products (PM). The energies shown in kcal/mol are relative to the reaction monomers (zero point). (G) Molecular structures of dimers produced by different reaction monomers and pathways. (H) DFT calculation of the interactions between the polymer chains, including two PIP-TMC molecular chains and two DPIP-TMC molecular chains, each containing three diamine and three TMC molecular components. The different colored regions among the polymer chains represent attraction (blue), van der Waals (green), and repulsion (red) interactions. (I) Gyration radius of polymer chains formed from diamine molecules with or without methyl groups. (J) Spatial distance between the geometric centers of polymer chains.

permeability of the selective layer was increased by the introduction of methyl groups. The SPI difference gradually decreased with increasing polyamide layer thickness due to its vertically asymmetric structure.[48] Further analysis revealed that the porosity in the selective layer (Figure 3E and Table S4), estimated using the Hagen−Poisseuille equation, increased from 1.8% for M_{PA} to 2.8−3.0% for M_{MPA} and M_{DPA}, demonstrating enhanced microporosity and explaining the

https://doi.org/10.1021/acs.est.5c16846
Environ. Sci. Technol. 2026, 60, 8823−8834

improvement of SPI. To further elucidate the microstructural changes, polyamide polymers were synthesized via a free IP process with different diamine monomers. The Brunauer−Emmett−Teller (BET) results showed that MPIP- and DPIP-prepared polymers contained numerous cavities with pore sizes larger than 0.6 nm (Figure 3F). Since amorphous organic polymer membranes transport solvents mainly through free volume and thermal movement of polymer chains, these additional cavities obviously reduce the solvent mass transfer resistance. Furthermore, we employed in situ positron annihilation spectroscopy (PAS) to characterize the evolution of the intrinsic free volume in the separation layer with and without methyl group introduction. The *S* parameter, defined as the ratio of counts in the central energy range (510.2−511.8 keV) to the total counts across the entire spectrum (499.5−522.5 keV), is a key indicator.[49,50] When more or larger free volumes exist within the material, positrons "trapped" within them are more likely to annihilate with low-momentum valence electrons. This process increases the counts in the central region of the energy spectrum, thereby raising the *S* parameter. As shown in Figure 3 G, M_{DPA}-0.2% and M_{DPA}-0.6% membranes exhibit higher *S* parameters, indicating that the introduction of methyl groups increases the number and size of the free volume in the separation layer, resulting in a more open polymer network. M_{DPA}-0.6% and M_{PA}-0.2% membranes exhibit similar effective pore sizes and thicknesses, yet M_{DPA}-0.6% demonstrates a higher *S* parameter value, further confirming the intrinsic enhancement in the free volume abundance. The *R* parameter is commonly used to define the separation layer range and characterize macroporous structures. Its marked increase corresponds to the boundary between the polyamide layer and the substrate membrane. The separation layer thickness relationship reflected by the *R* parameter aligns with AFM test data, validating the accuracy of our multimethod characterization (Figure 3H).

To better understand the internal microstructure of the membrane prepared with different monomers, MD simulations were performed to establish polymer models. The initial molar ratio of the reaction monomers was set according to the X-ray photoelectron spectroscopy (XPS) test results (Figure S11), followed by the cross-linking reaction and polymer relaxation and stabilization processes.[51] The fraction of free volume (FFV) of PIP-TMC is approximately 9.8% (Figure 3G), consistent with the simulation result reported in the literature[52] but higher than the calculated porosity in Figure 3E. This discrepancy arises because the actual transport path of water molecules in separation layer is highly tortuous and much larger than the apparent thickness of the separation layer (Figure S12). By the introduction of methyl groups, the FFV of MPIP-TMC and DPIP-TMC increased substantially to 16.7% and 18.9%, respectively (Figure 3H,I). Projection plots of the simulated polymers in different directions also showed significant structural differences (Figure S13). Correspondingly, the simulated polymer density decreased from 1.143 to 1.122 and 1.086 g cm^{-3}, respectively (Figure S14). In addition, the number and size of the internal cavities in the MPIP-TMC and DPIP-TMC polymers increased significantly compared to those in the PIP-TMC polymer (Figure S15).

The above data from MD, BET, and PAS consistently demonstrate an increase in the abundance of free volume within the polyamide following the introduction of methyl groups. Combined with the results of the SPI calculation, this increased free volume does not exist as isolated cavities but is interconnected, thereby enhancing the interconnectivity of the free volume network, actively participating in the effective transport of solvents within the polyamide, and increasing the material's intrinsic permeability. Although calculating the SPI based on the Hagen−Poiseuille equation simplifies the free volume network of the amorphous polyamide into a static pore network—an admitted oversimplification—it provides a simplified yet valuable framework for comparing and quantifying trends across different samples under identical assumptions, offering crucial insights into the evolution of the microstructure within the polyamide layer. More intuitive and direct characterization methods for free volume interconnectivity present significant challenges, motivating the exploration of novel approaches in future work.

Insight into the Interfacial Polymerization Reaction Mechanism and Polymer Chain Interactions

It is generally accepted that the diamine monomer diffuses across the water/oil interface to react with the TMC monomers in the IP process, with the trans-interfacial diffusion of diamine monomers often being the limiting step.[27,53] Therefore, understanding the diffusion and reaction properties of the monomers is essential to unraveling the synthesis−property relationships of the different reactive monomers.

MD simulations were performed to analyze the diffusion behavior of PIP, MPIP, and DPIP monomers using the diffusion model shown in Figure 4A and Figure S2. The diffusion information was collected when the system energy reached a steady state (Figure S16). The mean square displacement (MSD) of monomers in the *z*-direction is shown in Figure 4B, from which the diffusion coefficient (D) was calculated: 2.34×10^{-10}, 2.56×10^{-10}, and 3.37×10^{-10} m^{-2} s^{-1} for PIP, MPIP, and DPIP, respectively, indicating that MPIP and DPIP exhibit higher diffusivity owing to the introduction of methyl groups. The *z*-direction number density (ρ_N) distribution further shows that MPIP and DPIP, particularly DPIP, have higher relative densities at the water/hexane interface (Figure 4C and Figure S17). Additionally, DPIP exhibits a preaccumulation peak near the interface, ensuring a high flux of monomers toward the interface. These results are confirmed by the monomer number at the interface (Figure 4D). The trans-interfacial diffusion potential was evaluated by calculating the binding free energy ($E_{binding}$) of the diamine monomers with its surroundings at different positions (Figure 4E and Figure S18).[3] Thermodynamically, the transport of MPIP or DPIP from the aqueous phase to the interface is exothermic, meaning that aggregation at the interface is a spontaneous process. The total energy change during trans-interfacial diffusion follows the trend PIP > MPIP > DPIP, suggesting that monomers are more likely to enter the hexane phase if having methyl groups by reducing the associated Gibbs free energy barrier.

Density functional theory (DFT) calculations were conducted to quantify the reactivity of the amine groups in each diamine monomer with the acyl chlorine groups in TMC, considering only dimer formation. The introduction of methyl groups, as electron donors, into PIP molecules enhances the Lewis basicity of the adjacent amine group, thereby improving its nucleophilic substitution reaction.[36] However, the methyl group also produces a steric effect between the amine and acyl chlorine groups, hindering the polymerization reaction. Whether this promotes or hinders the amidation reaction remains to be judged. The calculation process was divided into

https://doi.org/10.1021/acs.est.5c16846
Environ. Sci. Technol. 2026, 60, 8823−8834

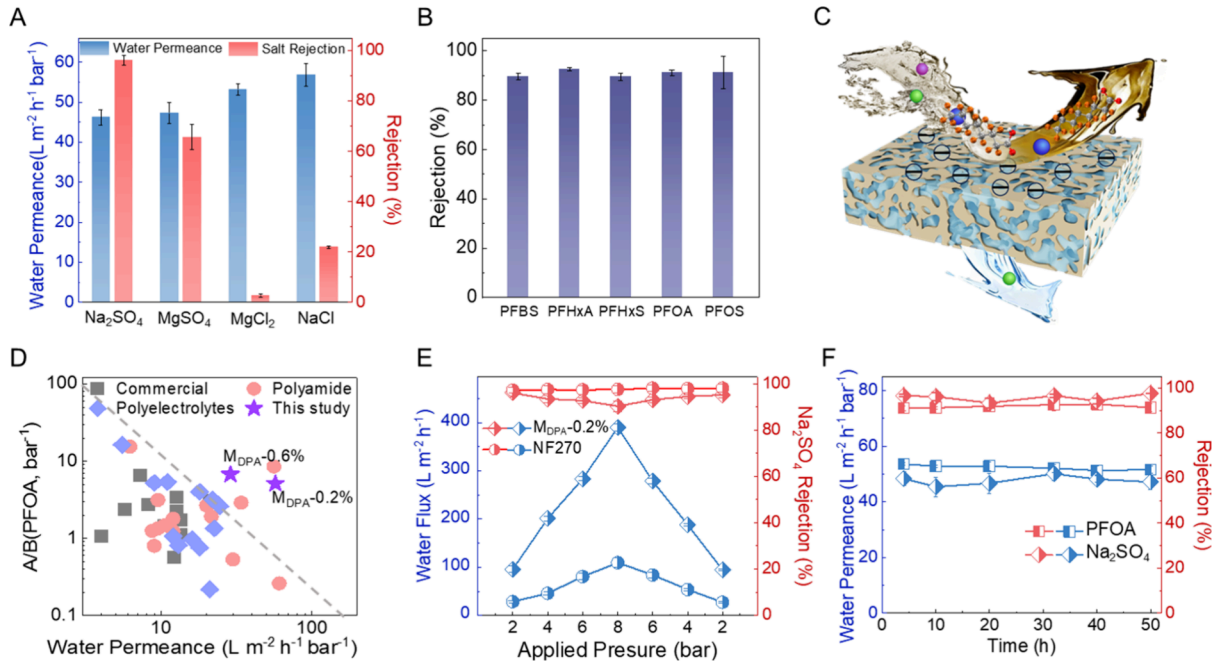

Figure 5. Filtration performance of the M_{DPA}-0.2% membrane. (A) Rejection of different salts and the corresponding water permeance under an ionic strength of 10 mmol L^{-1} salt solution and an applied pressure of 2 bar. (B) Rejection of five per- and polyfluoroalkyl substances with different molecular weights under an applied pressure of 2 bar and a concentration of 100 μg L^{-1} for each. (C) Schematic diagram of PFAS removal by a highly negative charged and hydrophilic NF membrane. (D) Relationship between PFOA rejection selectivity and water permeance. (E) Variation of membrane separation performance with applied pressure under an ionic strength of 10 mmol L^{-1} Na_2SO_4 solution, in comparison to NF270. (F) Stability of membrane separation performance with an operating time under 2 bar.

five stages, with the corresponding molecular structures shown in Figure 4G and Figure S19. The energy barrier (ΔG) for the reaction of the acyl chlorine group in TMC with the amine group of PIP is 6.41 kcal/mol, while the corresponding values for the $-N^{(1)}H$ group in MPIP and the amine group in DPIP are significantly higher, at 11.67 and 13.31 kcal/mol, respectively (Figure 4F). This suggests that the steric effect of the methyl group plays a more important role in the reaction, thereby weakening the reactivity of the amine group. The reaction potential energy (ΔE) (Figure S20), which reflects the polymerization reaction rate between monomers, aligns with the change in ΔG, indicating a decrease in the reaction rate after the introduction of methyl groups.

Furtherly, the intra- and interpolyamide molecular chain interactions were calculated by DFT.[54] After introducing methyl groups, the intrachain van der Waals interactions and the steric effects in the formed polypiperazine-amide chain are enhanced, hindering polymer chain agglomeration and curling (Figure S21). The structure of the PIP-TMC polymer chains in the equilibrium state shows significant twisting and rotation (Figure 4H), with the gyration radius of 13.17 ± 0.05 Å (Figure 4I) and the geometrically averaged distance between the molecular chains being about 3.9 Å (Figure 4J). In contrast, the interactions between DPIP-TMC polymer chains are rather weakened by the methyl groups (Figure 4H), with the gyration radius and the geometrically averaged distance between molecular chains increasing to 13.45 ± 0.06 and 6.1 Å, respectively. This indicates that the introduced methyl groups, serving as "molecular pillar" sites, significantly alter the interactions within/between polymer chains, thereby promoting an increase in free volume abundance and interconnectivity.

Based on these calculations, we conclude that compared to the reaction between PIP and TMC, the cross-linking degree of the polymer formed from methylated diamine monomers decreases due to the faster trans-interfacial diffusion and slower reaction kinetics, resulting in the formation of a thinner polypiperazine-amide layer with more linear polymer fragments. This is confirmed by the XPS data (Figure S11). The changes in diffusion and reaction properties facilitate the self-adaptation of the formed polymer chain structure during the polymerization process, and the increase in linearly structured fragments is more conducive to methyl groups playing the "molecular pillar" roles. Together, these effects contribute to a thinner separation layer with an enhanced free volume abundance and interconnectivity. While a reduced cross-linking degree favors the "molecular pillar" effect of methyl groups, it should be noted that excessively low cross-linking can compromise structural stability and selectivity.[55] As shown in Figure 3D, the SPI value of the M_{DPA}-0.2% membrane deviates from the fitted curve and is lower than that of the M_{DPA}-0.6% membrane, suggesting incipient structural deterioration at a very low cross-linking degree. This adverse effect is even more pronounced in M_{PA} membranes lacking the "molecular pillar" effect. For instance, the M_{PA}-0.1% membrane with a lower cross-linking degree (Figure S22) and thinner thickness exhibits much poorer separation performance than M_{PA}-0.2%. Therefore, it is crucial to achieve a balance between reducing the cross-linking degree to promote the role of methyl groups and maintaining polymer structural stability.

PFAS Removal Performance and Stability

The membrane separation performance was dramatically improved by introducing methyl groups into the polyamide molecular chains, particularly for the M_{DPA} membranes. These membranes exhibit high water permeability, excellent hydro-

https://doi.org/10.1021/acs.est.5c16846
Environ. Sci. Technol. 2026, 60, 8823−8834

philicity, and high negative charge density on the surface (Figure S23 and Figure S24), demonstrating promising potential for water treatment applications. The Na_2SO_4 rejection by M_{DPA}-0.2% is higher than 96%, while the $MgCl_2$ rejection is lower than 5% (Figure 5A). This substantial difference in rejection makes M_{DPA}-0.2% highly suitable for drinking water treatment to remove organic micropollutants such as PFAS, while retaining essential minerals in the treated water.[56] The removal rate of five PFAS (300−500 Da) exceeds 90% (Figure 5B), outperforming typical commercial NF270 membranes (Figure S25). Although the molecular weights of some PFAS are lower than the MWCO of M_{DPA}-0.2%, the strong negative charge and hydrophilicity of membrane enhance electrostatic repulsion and reduce hydrophobic interactions with PFAS, thus contributing to PFAS removal (Figure 5C).[57] We systematically measured the rejection of PFASs by the M_{DPA}-0.2% membrane at various NaCl concentrations. As the ionic strength increased, the rejection of all PFASs decreased to varying degrees. For example, the rejection of PFOS dropped from 96% at 5 mM NaCl to 84% at 50 mM NaCl, while that of the smaller PFBS decreased from 91% at 5 mM NaCl to 57% at 50 mM NaCl (Figure S26). This pronounced decrease in the level of rejection provides direct and unambiguous experimental evidence that electrostatic repulsion plays an important role under low ionic strength solution conditions. The PFOA rejection selectivity−water permeance relationship shows that M_{DPA} membranes have exceeded most literature-reported membranes and commercial NF membranes (Figure 5D, Figure S27, and Table S5).

Pressure stability tests were conducted with applied pressures up to 8 bar, and the water flux of M_{DPA}-0.2% showed direct proportionality to the applied pressure (Figure 5E). Although the Na_2SO_4 rejection slightly decreased with increasing applied pressure, the initial rejection was fully recovered when the pressure was removed, indicating no structural damage to the selective separation layer. The observed decrease in Na_2SO_4 rejection at a high pressure was attributed to concentration polarization, which is associated with the elevated water flux. The real Na_2SO_4 rejection after concentration polarization correction remains essentially unchanged under different pressures (Figure S28). Generally, since the practically employed water flux for NF processes is normally within 10−30 L m^{-2} h^{-1}, M_{DPA}-0.2% is expected to perform effectively at low pressure, without considering the compaction of the polyamide layer. This membrane can even be used in vacuum-driven processes, in lieu of microfiltration and ultrafiltration membranes, exemplified by the membrane bioreactor process, to improve the quality of treated water.[58] The membrane showed satisfactory operational stability with high perfluorooctanoic acid (PFOA) rejection and no significant deterioration in water permeance during a 50 h test (Figure 5F). Considering that DPIP-prepared membranes are fully compatible with the current NF membrane production lines, these membranes possess great potential for water treatment applications.

■ ENVIRONMENTAL IMPLICATIONS

Enhancing water permeability without sacrificing the rejection selectivity is key to reducing the operational energy consumption of NF systems, thereby promoting the widespread application of NF membranes in water treatment. This study developed a novel preparation strategy for high-permselectivity NF membranes featuring regulation of the nanostructure of the selective separation layer, particularly enhancing the free volume abundance and interconnectivity, by introducing methyl groups into the polypiperazine-amide molecular chains, which can effectively overcome the trade-off effect between water permeance and solute rejection while preserving the proven merits of conventional polypiperazine-amide materials. The "synthesis−properties−performance−applications" relationships of methylated piperazines have been systematically investigated, especially the effects of introducing methyl groups to PIP on trans-interfacial diffusion, monomer reactivity, and intra- and intermolecular interactions within the formed polymer chains. The M_{DPA}-0.2% membrane exhibited a high water permeance of 58 L m^{-2} h^{-1} bar^{-1} while maintaining excellent PFAS rejection (>90%). Furthermore, the M_{DPA}-0.6% membrane, possessing smaller pore size, achieved even higher PFAS rejection (>95%, Figure S29) and rejection stability (Figure S30). These results demonstrate the promising potential of these membranes for treating PFAS-contaminated water. Additionally, these membranes with high free volume interconnectivity can also be used for precise separation of solutes to recover resources. We evaluated the Cl^-/SO_4^{2-} separation selectivity of M_{DPA}-0.6%, which consistently demonstrated high SO_4^{2-} rejection and negative rejection of Cl^- ions under various conditions of high-concentration salt mixtures (Figure S31). This novel strategy, which enhances free volume interconnectivity through tailoring polymer chain interactions, will lead to a new wave of breakthroughs in the fabrication of high-permeability NF membranes.

More profoundly, the proposed strategy—modifying traditional piperazine or trimesoyl chloride monomers with functional groups—establishes a versatile molecular platform for the rational design of advanced functional membranes. This approach opens avenues for tailoring membranes with specific properties by leveraging diverse chemistries. For instance, introducing sulfonic acid groups can enhance surface charge for precise solute separation, while incorporating fluorine-containing moieties can significantly improve fouling resistance. The key to realizing such functional membranes lies in the strategic modification of reactive monomers, a process that will benefit from cross-disciplinary collaboration with experts in organic synthesis. Importantly, owing to its compatibility with conventional interfacial polymerization, any resulting membrane can be seamlessly integrated into existing manufacturing processes, ensuring excellent scalability. This study provides a foundational inspiration for developing next-generation polymeric membranes with customized permselectivity for targeted environmental and chemical separations.

■ ASSOCIATED CONTENT

Supporting Information

The Supporting Information is available free of charge at https://pubs.acs.org/doi/10.1021/acs.est.5c16846.

Details of materials and methods (Texts S1−S6); membrane filtration equipment diagram (Figure S1); molecular dynamics simulations model of monomers' diffusion processes (Figure S2); FTIR spectra (Figure S3); separation performance of membranes prepared using different monomers and concentrations (Figures S4−S6); comparison of membrane separation performance (Figures S7 and S8); surface roughness (Figure

https://doi.org/10.1021/acs.est.5c16846
Environ. Sci. Technol. 2026, 60, 8823−8834

S9); thickness of a polyamide layer (Figure S10); XPS spectrum (Figure S11); SEM image of the substrate UF membrane (Figure S12); molecular dynamics simulations of polymer structures (Figures S13−S15); molecular dynamics simulations of monomers' diffusion processes (Figures S16−S18); molecular structure diagrams and reaction potential energy of the reaction monomers at different reaction stages (Figures S19 and S20); interactions within the molecular chain (Figure S21); XPS results of M_{PA}-0.1% (Figure S22); water contact angle (Figure S23); zeta potential of the membrane surface (Figure S24); PFAS rejection of NF270 (Figure S25); PFAS rejection of M_{DPA}-0.2% under different salt concentrations (Figure S26); PFOA rejection of membranes in the reported literature (Figure S27); real Na_2SO_4 rejection after concentration polarization correction (Figure S28); PFAS rejection of M_{DPA}-0.6% (Figure S29); separation stability of M_{DPA}-0.6% (Figure S30); Cl^-/SO_4^{2-} separation performance (Figure S31); PFAS information (Table S1); separation properties of commercial membranes (Table S2); separation performance of advanced membranes reported in the literature (Table S3); membrane structure parameters for porosity calculations (Table S4); PFOA rejection of advanced membranes reported in the literature (Table S5) (PDF)

AUTHOR INFORMATION

Corresponding Authors

Xiao-mao Wang − *State Key Laboratory of Regional Environment and Sustainability, School of Environment, Tsinghua University, Beijing 100084, China;* orcid.org/0000-0003-2907-3951; Phone: (+86-10) 6278-1386; Email: wangxiaomao@tsinghua.edu.cn

Xia Huang − *State Key Laboratory of Regional Environment and Sustainability, School of Environment, Tsinghua University, Beijing 100084, China;* orcid.org/0000-0003-4076-1464; Phone: (+86-10) 6277-2324; Email: xhuang@tsinghua.edu.cn

Authors

Kunpeng Wang − *State Key Laboratory of Regional Environment and Sustainability, School of Environment, Tsinghua University, Beijing 100084, China*

Haiyang He − *State Key Laboratory of Regional Environment and Sustainability, School of Environment, Tsinghua University, Beijing 100084, China*

Xingzhong Cao − *Institution of High Energy Physics, Chinese Academy of Sciences, Beijing 100049, China;* orcid.org/0000-0001-5011-5912

Danyang Li − *State Key Laboratory of Regional Environment and Sustainability, School of Environment, Tsinghua University, Beijing 100084, China*

Yanling Liu − *State Key Laboratory of Pollution Control and Resources Reuse, College of Environmental Science and Engineering, Tongji University, Shanghai 200092, China;* orcid.org/0000-0003-0856-9632

Wenkai Liu − *State Key Laboratory of Regional Environment and Sustainability, School of Environment, Tsinghua University, Beijing 100084, China*

Peng Liang − *State Key Laboratory of Regional Environment and Sustainability, School of Environment, Tsinghua University, Beijing 100084, China;* orcid.org/0000-0001-7345-0844

Complete contact information is available at: https://pubs.acs.org/10.1021/acs.est.5c16846

Notes

The authors declare no competing financial interest.

ACKNOWLEDGMENTS

We acknowledge support by the National Natural Science Foundation of China (Nos. 52400089 and 52270007), the China Postdoctoral Science Foundation (2025M771278), the China State-sponsored Postdoctoral Researcher Program Grade B (No. GZB20240350), and the "Shuimu Tsinghua Scholar" Program of Tsinghua University.

REFERENCES

(1) Epsztein, R.; DuChanois, R. M.; Ritt, C. L.; Noy, A.; Elimelech, M. Towards Single-Species Selectivity of Membranes with Sub-nanometre Pores. *Nat. Nanotechnol.* **2020**, *15*, 426−436.

(2) Zhang, H.; He, Q.; Luo, J.; Wan, Y.; Darling, S. B. Sharpening Nanofiltration: Strategies for Enhanced Membrane Selectivity. *ACS Appl. Mater. Interfaces* **2020**, *12*, 39948−39966.

(3) Liang, Y.; Zhu, Y.; Liu, C.; Lee, K. R.; Hung, W. S.; Wang, Z.; Li, Y.; Elimelech, M.; Jin, J.; Lin, S. Polyamide Nanofiltration Membrane with Highly Uniform Sub-nanometre Pores for Sub-1 Å Precision Separation. *Nat. Commun.* **2020**, *11*, 2015.

(4) Liu, Y.; Wang, K.; Zhou, Z.; Wei, X.; Xia, S.; Wang, X.; Xie, Y. F.; Huang, X. Boosting the Performance of Nanofiltration Membranes in Removing Organic Micropollutants: Trade-Off Effect, Strategy Evaluation, and Prospective Development. *Environ. Sci. Technol.* **2022**, *56*, 15220−15237.

(5) Luo, J.; Zhou, B.; Xue, N.; Han, Y.; Liu, W.; He, T. Interaction of Layer-by-Layer Nanofiltration Membranes and PFAS: Filtration after Adsorption. *Environ. Sci. Technol.* **2025**, *59*, 15481−15492.

(6) Li, S.; Ding, J.; Liu, Z.; Jia, J.; Zhao, Q.; Li, P.; Zhang, H.; Li, G.; Bai, L.; Liang, H. Interface-Facilitated Removal of Environmental Micropollutants by Nanofiltration Membranes Prepared from Amino Acid-Mediated Interfacial Polymerization: Mechanistic Insights into Micropollutant Interfacial Partitioning Regulation. *Environ. Sci. Technol.* **2025**, *59*, 13085−13095.

(7) Wang, K.; Wang, X.; Januszewski, B.; Liu, Y.; Li, D.; Fu, R.; Elimelech, M.; Huang, X. Tailored Design of Nanofiltration Membranes for Water Treatment Based on Synthesis−Property−Performance Relationships. *Chem. Soc. Rev.* **2022**, *51*, 672−719.

(8) Lu, X.; Elimelech, M. Fabrication of Desalination Membranes by Interfacial Polymerization: History, Current Efforts, and Future Directions. *Chem. Soc. Rev.* **2021**, *50*, 6290−6307.

(9) Liu, C.; Yang, J.; Guo, B.; Agarwal, S.; Greiner, A.; Xu, Z. Interfacial Polymerization at the Alkane/Ionic Liquid Interface. *Angew.Chem. Int. Ed.* **2021**, *60*, 14636−14643.

(10) Park, H. B.; Kamcev, J.; Robeson, L. M.; Elimelech, M.; Freeman, B. D. Maximizing the Right Stuff: the Trade-off Between Membrane Permeability and Selectivity. *Science* **2017**, *356*, No. eaab0530.

(11) Yang, Z.; Long, L.; Wu, C.; Tang, C. Y. High Permeance or High Selectivity? Optimization of System-Scale Nanofiltration Performance Constrained by the Upper Bound. *ACS ES&T Engineering* **2022**, *2*, 377−390.

(12) Karan, S.; Jiang, Z.; Livingston, A. G. Sub−10 nm Polyamide Nanofilms with Ultrafast Solvent Transport for Molecular Separation. *Science* **2015**, *348*, 1347−1351.

(13) Zhu, X.; Cheng, X.; Luo, X.; Liu, Y.; Xu, D.; Tang, X.; Gan, Z.; Yang, L.; Li, G.; Liang, H. Ultrathin Thin-Film Composite Polyamide Membranes Constructed on Hydrophilic Poly(vinyl alcohol)

Decorated Support Toward Enhanced Nanofiltration Performance. *Environ. Sci. Technol.* **2020**, *54*, 6365−6374.
(14) Sarkar, P.; Wu, C.; Yang, Z.; Tang, C. Y. Empowering Ultrathin Polyamide Membranes at the Water−Energy Nexus: Strategies, Limitations, and Future Perspectives. *Chem. Soc. Rev.* **2024**, *53*, 4374−4399.
(15) Zhang, R.; Tian, J.; Gao, S.; van der Bruggen, B. How to Coordinate the Trade-off Between Water Permeability and Salt Rejection in Nanofiltration? *J. Mater. Chem. A* **2020**, *8*, 8831−8847.
(16) Tan, Z.; Chen, S.; Peng, X.; Zhang, L.; Gao, C. Polyamide Membranes with Nanoscale Turing Structures for Water Purification. *Science* **2018**, *360*, 518−521.
(17) Liu, S. H.; Shi, W.; Hung, W. S.; Shi, L.; Xue, B.; She, J.; Song, Z.; Lu, X.; Gray, S.; Lee, K. R.; Wu, C. Interfacial Self-Organization of Large-Area Mixed-Dimensional Polyamide Membranes for Rapid Aqueous Nanofiltration. *Nat. Water* **2024**, *2*, 1238−1248.
(18) Dai, R.; Zhou, H.; Wang, T.; Qiu, Z.; Long, L.; Lin, S.; Tang, C. Y.; Wang, Z. Nanovehicle-Assisted Monomer Shuttling Enables Highly Permeable and Selective Nanofiltration Membranes for Water Purification. *Nat. Water* **2023**, *1*, 281−290.
(19) Wang, Z.; Wang, Z.; Lin, S.; Jin, H.; Gao, S.; Zhu, Y.; Jin, J. Nanoparticle-Templated Nanofiltration Membranes for Ultrahigh Performance Desalination. *Nat. Commun.* **2018**, *9*, 2004.
(20) Jiang, C.; Tian, L.; Zhai, Z.; Shen, Y.; Dong, W.; He, M.; Hou, Y.; Niu, Q. J. Thin-Film Composite Membranes with Aqueous Template-Induced Surface Nanostructures for Enhanced Nanofiltration. *J. Membr. Sci.* **2019**, *589*, No. 117244.
(21) Han, S.; Zhu, J.; Uliana, A. A.; Li, D.; Zhang, Y.; Zhang, L.; Wang, Y.; He, T.; Elimelech, M. Microporous Organic Nanotube Assisted Design of High Performance Nanofiltration Membranes. *Nat. Commun.* **2022**, *13*, 7954.
(22) Lim, Y. J.; Goh, K.; Wang, R. The Coming of Age of Water Channels for Separation Membranes: from Biological to Biomimetic to Synthetic. *Chem. Soc. Rev.* **2022**, *51*, 4537−4582.
(23) Culp, T. E.; Khara, B.; Brickey, K. P.; Geitner, M.; Zimudzi, T. J.; Wilbur, J. D.; Jons, S. D.; Roy, A.; Paul, M.; Ganapathysubramanian, B.; Zydney, A. L.; Kumar, M.; Gomez, E. D. Nanoscale Control of Internal Inhomogeneity Enhances Water Transport in Desalination Membrane. *Science.* **2021**, *371*, 72−75.
(24) Jimenez-Solomon, M. F.; Song, Q.; Jelfs, K. E.; Munoz-Ibanez, M.; Livingston, A. G. Polymer Nanofilms with Enhanced Microporosity by Interfacial Polymerization. *Nat. Mater.* **2016**, *15*, 760−767.
(25) Jiang, C.; Tian, L.; Hou, Y.; Niu, Q. J. Nanofiltration Membranes with Enhanced Microporosity and Inner-Pore Interconnectivity for Water Treatment: Excellent Balance Between Permeability and Selectivity. *J. Membr. Sci.* **2019**, *586*, 192−201.
(26) Ge, L.; Li, J.; Du, G.; Sheng, K.; Hou, J.; Zhou, B.; Zhang, Y.; van der Bruggen, B.; Zhu, J. Microporous Polyacylhydrazone Membranes with 3D Interconnected Nanochannels for Accurate Molecular Sieving. *Adv. Funct. Mater.* **2025**, *35*, No. 2504997.
(27) Freger, V.; Ramon, G. Z. Polyamide Desalination Membranes: Formation, Structure, and Properties. *Prog. Polym. Sci.* **2021**, *122*, No. 101451.
(28) Liu, C.; Zhu, C.; Zhang, C.; Yang, H.; Xu, Z. Thermodynamic and Kinetic Understanding for Managing the Controllability of Interfacial Polymerization. *Prog. Polym. Sci.* **2024**, *152*, No. 101815.
(29) Freger, V. Nanoscale Heterogeneity of Polyamide Membranes Formed by Interfacial Polymerization. *Langmuir* **2003**, *19*, 4791−4797.
(30) Liu, Y.; Liu, L.; Narendra, B.; Chen, X.; Feng, S.; Wan, Y.; Luo, J. Advancing High-Performance Nanoffltration Membranes: Tailoring Monomer Molecular Design to Enhance Diffusion-Reaction Synergy in Interfacial Polymerization. *Desalination* **2025**, *598*, No. 118415.
(31) Kim, S. H.; Kwak, S. Y.; Suzuki, T. Positron Annihilation Spectroscopic Evidence to Demonstrate the Flux-Enhancement Mechanism in Morphology-Controlled Thin-Film-Composite (TFC) Membrane. *Environ. Sci. Technol.* **2005**, *39*, 1764−1770.
(32) Liu, S.; Ganti-Agrawal, S.; Keten, S.; Lueptow, R. M. Molecular Insights Into Charged Nanofiltration Membranes: Structure, Water transport, and Water diffusion. *J. Membr. Sci.* **2022**, *644*, No. 120057.
(33) Shen, L.; Cheng, R.; Yi, M.; Hung, W. S.; Japip, S.; Tian, L.; Zhang, X.; Jiang, S.; Li, S.; Wang, Y. Polyamide-Based Membranes with Structural Homogeneity for Ultrafast Molecular Sieving. *Nat. Commun.* **2022**, *13*, 500.
(34) Ali, Z.; Ghanem, B. S.; Wang, Y.; Pacheco, F.; Ogieglo, W.; Vovusha, H.; Genduso, G.; Schwingenschlögl, U.; Han, Y.; Pinnau, I. Finely Tuned Submicroporous Thin-Film Molecular Sieve Membranes for Highly Efficient Fluid Separations. *Adv. Mater.* **2020**, *32*, No. 2001132.
(35) Soyekwo, F.; Liu, C.; Mao, X.; Shi, X. Poly(bis(1-methylpiperazin-1-ium-amide) Nanofilm Composite Membrane with Nanochannel-Enabled Microporous Structure and Enhanced Steric Hindrance for Magnesium/Lithium Separation. *Adv. Funct. Mater.* **2024**, *35*, No. 2412463.
(36) Yao, Y.; Zhang, P.; Sun, F.; Zhang, W.; Li, M.; Sha, G.; Teng, L.; Wang, X.; Huo, M.; DuChanois, R. M.; Cao, T.; Boo, C.; Zhang, X.; Elimelech, M. More Resilient Polyester Membranes for High-Performance Reverse Osmosis Desalination. *Science* **2024**, *384*, 333−338.
(37) Jiang, Z.; Dong, R.; Evans, A. M.; Biere, N.; Ebrahim, M. A.; Li, S.; Anselmetti, D.; Dichtel, W. R.; Livingston, A. G. Aligned Macrocycle Pores in Ultrathin Films for Accurate Molecular Sieving. *Nature* **2022**, *609*, 58−64.
(38) Yang, Z.; Guo, H.; Tang, C. Y. The upper bound of thin-film composite (TFC) polyamide membranes for desalination. *J. Membr. Sci.* **2019**, *590*, No. 117297.
(39) Lu, X.; Wang, L.; Peng, H.; Zhu, X.; Yang, Z.; Wei, J.; Liu, B. Double nanofoaming enhanced interfacial polymerization toward ultra-high-performance nanofiltration membranes. *Environ. Sci. Technol.* **2025**, *59*, 19593−19603.
(40) Abraham, M. J.; Murtola, T.; Schulz, R.; Pall, S.; Smith, J. C.; Hess, B.; Lindahl, E. GROMACS: High Performance Molecular Simulations through Multi-Level Parallelism from Laptops to Supercomputers. *SoftwareX* **2015**, *1−2*, 19−25.
(41) Hess, B. P-LINCS: A Parallel Linear Constraint Solver for Molecular Simulation. *J. Chem. Theory Comput.* **2008**, *4*, 116−122.
(42) Hess, B.; Bekker, H.; Berendsen, H. J. C.; Fraaije, J. G. E. M. LINCS: a Linear Constraint Solver for Molecular Simulations. *J. Comput. Chem.* **1997**, *18*, 1463−1472.
(43) Darden, T.; York, D.; Pedersen, L. Particle Mesh Ewald: an N·log(N) Method for Ewald Sums in Large Systems. *J. Chem. Phys.* **1993**, *98*, 10089−10092.
(44) Willems, T. F.; Rycroft, C.; Kazi, M.; Meza, J. C.; Haranczyk, M. Algorithms and Tools for High-Throughput Geometry-Based Analysis of Crystalline Porous Materials. *Microporous Mesoporous Mater.* **2012**, *149*, 134−141.
(45) Frisch, M. J.; Trucks, G. W.; Schlegel, H. B.; Scuseria, G. E.; Robb, M. A.; Cheeseman, J. R.; Scalmani, G.; Barone, V.; Petersson, G. A.; Nakatsuji, H.; Li, X.; Caricato, M.; Marenich, A. V.; Bloino, J.; Janesko, B. G.; Gomperts, R.; Mennucci, B.; Hratchian, H. P.; Ortiz, J. V.; Izmaylov, A. F.; Sonnenberg, J. L.; Williams-Young, D.; Ding, F.; Lipparini, F.; Egidi, F.; Goings, J.; Peng, B.; Petrone, A.; Henderson, T.; Ranasinghe, D.; Zakrzewski, V. G.; Gao, J.; Rega, N.; Zheng, G.; Liang, W.; Hada, M.; Ehara, M.; Toyota, K.; Fukuda, R.; Hasegawa, J.; Ishida, M.; Nakajima, T.; Honda, Y.; Kitao, O.; Nakai, H.; Vreven, T.; Throssell, K.; Montgomery, J. A., Jr.; Peralta, J. E.; Ogliaro, F.; Bearpark, M. J.; Heyd, J. J.; Brothers, E. N.; Kudin, K. N.; Staroverov, V. N.; Keith, T. A.; Kobayashi, R.; Normand, J.; Raghavachari, K.; Rendell, A. P.; Burant, J. C.; Iyengar, S. S.; Tomasi, J.; Cossi, M.; Millam, J. M.; Klene, M.; Adamo, C.; Cammi, R.; Ochterski, J. W.; Martin, R. L.; Morokuma, K.; Farkas, O.; Foresman, J. B.; Fox, D. J. *Gaussian 16*; Gaussian, Inc.: Wallingford, CT, 2016.
(46) Lu, T.; Chen, F. Multiwfn: a Multifunctional Wavefunction Analyzer. *J. Comput. Chem.* **2012**, *33*, 580−592.
(47) Shao, S.; Zeng, F.; Long, L.; Zhu, X.; Peng, L. E.; Wang, F.; Yang, Z.; Tang, C. Y. Nanofiltration Membranes with Crumpled

https://doi.org/10.1021/acs.est.5c16846
Environ. Sci. Technol. 2026, 60, 8823−8834

Polyamide Films: a Critical Review on Mechanisms, Performances, and Environmental Applications. *Environ. Sci. Technol.* **2022**, *56*, 12811−12827.
(48) Coronell, O.; Marinas, B. J.; Cahill, D. G. Depth Heterogeneity of Fully Aromatic Polyamide Active Layers in Reverse Osmosis and Nanofiltration Membranes. *Environ. Sci. Technol.* **2011**, *45*, 4513−4520.
(49) Wang, P.; Ma, Y.; Qin, X.; Zhang, Z.; Cao, X.; Yu, R.; Wang, B. Performance of the plugged-in ^{22}Na Based slow positron beam facility. *Chin. Phys. C* **2008**, *32*, 243−246.
(50) Wang, K.; Fu, W.; Wang, X.; Xu, C.; Gao, Y.; Liu, Y.; Zhang, X.; Huang, X. Molecular Design of the Polyamide Layer Structure of Nanofiltration Membranes by Sacrificing Hydrolyzable Groups toward Enhanced Separation Performance. *Environ. Sci. Technol.* **2022**, *56*, 17955−17964.
(51) Zhang, H.; Wu, M. S.; Zhou, K.; Law, A. W. K. Molecular Insights into the Composition−Structure−Property Relationships of Polyamide Thin Films for Reverse Osmosis Desalination. *Environ. Sci. Technol.* **2019**, *53*, 6374−6382.
(52) Peng, H.; Liu, X.; Su, Y.; Li, J.; Zhao, Q. Advanced Lithium Extraction Membranes Derived from Tagged-Modification of Polyamide Networks. *Angew. Chem., Int. Ed.* **2023**, *62*, No. e202312795.
(53) Zhang, F.; Fan, J.; Wang, S. Interfacial Polymerization: from Chemistry to Functional Materials. *Angew. Chem., Int. Ed.* **2020**, *59*, 21840−21856.
(54) Lu, T.; Chen, Q. Visualization Analysis of Weak Interactions in Chemical Systems. In *Comprehensive Computational Chemistry*, Yáñez, M.; Boyd, R. J., Eds., Elsevier, 2024, Vol. 2, pp 240−264.
(55) Lan, X.; Liu, Y.; Chen, X.; Feng, S.; Wan, Y.; Luo, J. Crosslinking Degree of Polyamide Membranes: From Determination to Rational Design. *Desalination* **2026**, *623*, No. 119760.
(56) Lu, X.; Wang, L.; Zhu, X.; Qiu, L.; Yang, Z.; Xu, D.; Wei, J.; Zhang, Q.; Chen, C.; Niu, S.; Liu, B. Unveiling Decrosslinking Degree on Polyamide Nanofiltration Membranes: Structure−Performance Relationship and Micropollutant Removal. *Water Res.* **2026**, *288*, No. 124763.
(57) Boo, C.; Wang, Y.; Zucker, I.; Choo, Y.; Osuji, C. O.; Elimelech, M. High Performance Nanofiltration Membrane for Effective Removal of Perfluoroalkyl Substances at High Water Recovery. *Environ. Sci. Technol.* **2018**, *52*, 7279−7288.
(58) Gan, B.; Peng, L. E.; Liu, W.; Zhang, L.; Wang, L. A.; Long, L.; Guo, H.; Song, X.; Yang, Z.; Tang, C. Y. Ultra-Permeable Silk-Based Polymeric Membranes for Vacuum-Driven Nanofiltration. *Nat. Commun.* **2024**, *15*, 8656.

https://doi.org/10.1021/acs.est.5c16846
Environ. Sci. Technol. 2026, 60, 8823−8834